ATLAS NOTE

ATLAS-CONF-2015-054

26th September 2015

Femtoscopy with identified charged pions in proton-lead collisions at $\sqrt{s_{\mathrm{NN}}} = 5.02$ TeV with ATLAS

The ATLAS Collaboration

Abstract

Bose-Einstein correlations between identified charged pions are measured for p+Pb collisions at $\sqrt{s_{\mathrm{NN}}} = 5.02$ TeV with the ATLAS detector with a total integrated luminosity of 28 nb^{-1}. Pions are identified using ionisation energy loss measured in the pixel detector. Two-particle correlation functions and the extracted source radii are presented as a function of average transverse pair momentum (k_{T}) and collision centrality. Pairs are selected with a pseudorapidity between -1.5 and 1.5 and with an average transverse momentum $0.1 < k_{\mathrm{T}} < 0.8$ GeV. The effect on the two-particle correlation function from jet fragmentation is studied, and a new method for constraining its contributions to the measured correlations is described. The measured source sizes are substantially larger in more central collisions and are observed to decrease with increasing pair k_{T}. Linear scaling of the volume with the average multiplicity in the acceptance region $|\eta| < 1.5$ is observed. The scaling of the extracted radii with the mean number of participants is also used to compare a selection of initial-geometry models.

ATLAS-CONF-2015-054
28 September 2015

1 Introduction

While hydrodynamic models are applied successfully to nucleus-nucleus (A+A) collisions, the extent to which they can describe p+Pb collisions remains a topic of active debate. Femtoscopy, the method of using final-state interactions to probe the space-time extent of a particle-emitting source, provides important input to this discussion [1].

Correlation functions of outgoing particle pairs are often studied in A+A collisions as a function of relative pseudorapidity ($\Delta\eta$) and azimuthal angle ($\Delta\phi$). For $|\Delta\eta| \gtrsim 2$ the jet contribution does not appear, and the correlation function $C(\Delta\eta, \Delta\phi)$ is then seen to be independent of $\Delta\eta$ [2–7]. These long-range correlations are known as the "ridge". The pair production is often decomposed into Fourier modes: $dN/d\Delta\phi \sim 1 + 2\Sigma_n v_n(p_T^a) v_n(p_T^b) \cos(n\Delta\phi)$. The measured v_n components are consistent with hydrodynamic evolution.

Recent observations of the ridge in p+Pb [8–10] and pp [11, 12] collisions, where the system size is much smaller than in Pb+Pb, raise questions over the interpretation of the v_n as being purely of hydrodynamic origin. Both hydrodynamic [13–16] and initial-state [17–21] models, as well as a hybrid scenario [22], are able to describe the observed v_2 and v_3 in p+Pb collisions.

The Hanbury Brown and Twiss (often abbreviated as "HBT") method originated in astronomy [23, 24], where space-time correlations of photons due to wavefunction symmetrisation are used to measure the size of distant stars. The procedure can be adapted to the tiny sources encountered in hadronic collisions if identical-particle Bose-Einstein correlations are instead studied in relative momentum space [25]. Measurements of these Bose-Einstein correlations in pp collisions at $\sqrt{s} = 0.9$ GeV and $\sqrt{s} = 7$ GeV have been produced by ATLAS [26], CMS [27], and ALICE [28]. At both energies the source radii are observed to decrease with rising transverse pair momentum k_{T}. It is also observed that the radii increase with particle multiplicity but saturate at the highest multiplicities.

Although Bose-Einstein correlations are the most straightforward to measure experimentally, any non-trivial interaction can be used in principle to image the source density. The term *femtoscopy* is often used to refer to any measurement that provides spatio-temporal information about a hadronic source [29]. The measured source radii are interpreted as the dimensions of a nuclear source at freeze-out, after all interactions between final-state particles and the bulk have ceased; thus, they are sensitive to the space-time evolution of the event. In particular, an increase in radii at low momentum indicates radial expansion since higher momentum particles are more likely to be produced earlier in the event [30]. The results of femtoscopic measurements in p+Pb systems are of significant interest because they can provide insight into the extent to which hydrodynamics applies in such small systems. While femtoscopic methods have already been applied to p+Pb systems at the LHC [31, 32], this analysis presents new data-driven techniques to constrain the significant background contribution from jet fragmentation, referred to in this note as the "hard process" background.

The results presented in this analysis are shown for collision centralities ranging from 0% to 80%, in centrality intervals no greater than 10% (see Sect. 3.1 for centrality definition). For a pair's average four-momentum k, the pair pseudorapidity η_k is selected from $|\eta_k| < 1.5$ and the results are shown as a function of transverse pair momentum 0.1 GeV $< k_{\mathrm{T}} <$ 0.8 GeV. One- and three-dimensional source radii are presented as a function of the average charged-particle multiplicity, and the scaling of the system size with the number of initial nucleon participants is also investigated, using the predictions of three initial-geometry models.

2 ATLAS detector

The ATLAS detector is described in detail in Ref. [33]. The inner detector (ID), which is immersed in a 2 Tesla axial magnetic field, is used to reconstruct charged particles within $|\eta| < 2.5$ [1]. It consists of a silicon pixel detector, a semi-conductor tracker (SCT) made of double-layered silicon microstrips, and a transition radiation tracker made of straw tubes. A particle travelling from the interaction point with $|\eta| < 2$ crosses at least 3 pixel layers, 4 double-sided micro-strip layers and typically 36 straw tubes.

The forward calorimeter (FCal), covering a pseudorapidity region of $3.1 < |\eta| < 4.9$, is used to measure the centrality of each collision. The FCal uses liquid argon as the active medium with tungsten and copper absorbers.

The Minimum Bias Trigger Scintillators (MBTS), consisting of two arrays of scintillation counters, are positioned at $z = \pm 3.6$ m and cover $2.1 < |\eta| < 3.9$. They are used for the MinBias Level-1 trigger [34] as well as to impose a constraint on the event selection.

3 Data analysis

3.1 Event and track selection

This analysis uses data from the LHC 2013 p+Pb run at $\sqrt{s_{\mathrm{NN}}} = 5.02$ TeV with an integrated luminosity of 28.1 nb^{-1}. The Pb ions had an energy per nucleon of 1.57 TeV and collided with the 4 TeV proton beam to yield a centre-of-mass energy $\sqrt{s_{\mathrm{NN}}} = 5.02$ TeV with a longitudinal rapidity boost of 0.465 in the proton direction relative to the ATLAS laboratory frame. Events are required to satisfy the Level-1 MinBias trigger and to have a hit on each side of the MBTS. The difference in time between the activity in each side can be no greater than 10 ns. Only a single reconstructed primary vertex (PV) is allowed, which is required to have at least two good tracks. Events which have more than one reconstructed vertex (including secondary vertices) with either more than 10 tracks or a scalar sum of track p_{T} greater than 6 GeV are rejected.

Event centrality is determined following the procedure in Ref. [35], using the total transverse energy in the Pb-going side of the FCal. The use of the FCal for measuring centrality has the advantage that it is not sensitive to multiplicity fluctuations in the kinematic region covered by the inner detector, where the femtoscopic measurement is performed. For each centrality interval the average charged-particle multiplicity $\langle dN_{\mathrm{ch}}/d\eta \rangle$ is measured and the corresponding average number of participating nucleons $\langle N_{\mathrm{part}} \rangle$ is derived using methods and data also described in Ref. [35]. Since this analysis uses finer centrality intervals (no wider than 10%), a linear interpolation is used to construct new values based on the published results. The values and errors from this procedure are tabulated in Sect. 6.2.

Reconstructed tracks, taken from $|\eta| < 2.5$ at $p_{\mathrm{T}} > 0.1$ GeV, must originate from hits near the interaction point. A minimum of one pixel hit is required, and if the track crosses an active module in the innermost layer, a hit in that layer is required. For a track p_{T} greater than 0.1, 0.2, or 0.3 GeV there must be at least 2, 4, or 6 hits in the SCT, respectively. The transverse impact parameter with respect to the primary vertex,

[1] ATLAS uses a right-handed coordinate system with its origin at the nominal interaction point (IP) in the centre of the detector and the z-axis along the beam pipe. The x-axis points from the IP to the centre of the LHC ring, and the y-axis points upward. Cylindrical coordinates (r, ϕ) are used in the transverse plane, ϕ being the azimuthal angle around the beam pipe. The pseudorapidity is defined in terms of the polar angle θ as $\eta = -\ln\tan(\theta/2)$.

d_0^{PV}, must be such that $|d_0^{\mathrm{PV}}| < 1.5$ mm. The corresponding longitudinal impact parameter must satisfy $|z_0^{\mathrm{PV}} \sin\theta| < 1.5$ mm. Neither $|d_0^{\mathrm{PV}}|$ nor $|z_0^{\mathrm{PV}} \sin\theta|$ can be larger than 3 times its uncertainty as derived from the covariance matrix of the track parameter fit.

3.2 Particle identification

Particle identification (PID) is performed through measurements of the energy loss dE/dx acquired from the ionization charge deposited in the pixel clusters crossed by a track. Relative likelihoods that the track is a π, K, and p are formed by fitting the dE/dx distributions to $\sqrt{s} = 7$ TeV pp data in several momentum intervals [36]. Three PID selection levels are defined: one designed to have a high efficiency for pions, one designed to result in high purity, and a middle ground which was chosen as the nominal selection level. The efficiency and purity of these selections are studied in a p+Pb sample generated using Hijing [37] and simulated with the GEANT4 package [38]. The sample is reconstructed with the same conditions as the data. The resulting purity of pairs in the nominal selection is shown in Fig. 1. The results are also evaluated at the looser and tighter PID definitions, and the variation is incorporated into the systematic uncertainty.

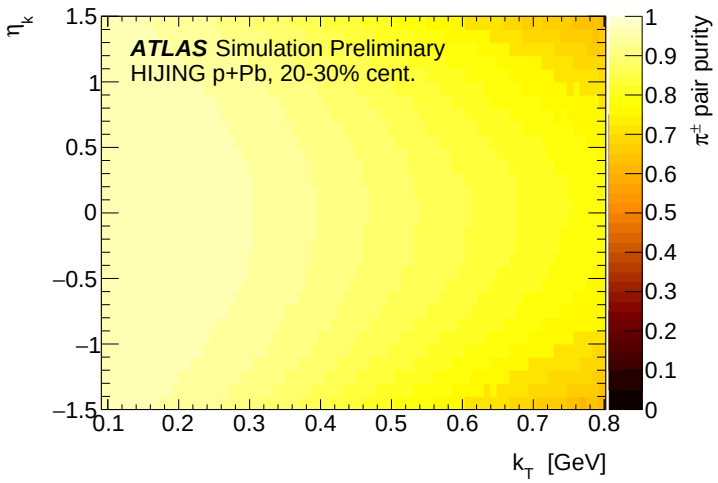

Figure 1: Purity of identified pion pairs, from fully simulated Hijing p+Pb events, as a function of the pair's average transverse momentum k_{T} and pseudorapidity η_k.

3.3 Pair selection

Track pairs are required to have $|\Delta\phi| < \pi/2$ to avoid an enhancement in the correlation function arising primarily from dijets. This enhancement is not present in the signal region but can influence the results by affecting the overall normalization factor in the fits. For a pair's average momentum $k = \frac{1}{2}\left(p^a + p^b\right)$ the pseudorapidity η_k must lie inside $|\eta_k| < 1.5$ (a narrower window than the track selection of $|\eta| < 2.5$). When analyzing track pairs of opposite sign, selections on the invariant mass are applied such that $\left|m_{\pi\pi} - m_{\rho^0}\right| > 150$ MeV, $\left|m_{\pi\pi} - m_{K^0_{\mathrm{S}}}\right| > 20$ MeV, and $\left|m_{KK} - m_{\phi(1020)}\right| > 20$ MeV, where m_{ab} is the pair's invariant mass calculated with particle masses m_a and m_b. These selections are applied when forming both the same- and mixed-event distributions.

3.4 Correlation function

The two-particle correlation function is defined as the ratio of two-particle and single-particle momentum spectra:

$$C\left(p^a, p^b\right) \equiv \frac{\frac{dN^{ab}}{d^3p^a d^3p^b}}{\frac{dN^a}{d^3p^a}\frac{dN^b}{d^3p^b}}, \tag{1}$$

for pairs of particles with four-momenta p^a and p^b. Utilising the correlation function as defined in this way has the experimental advantage that most of the single-particle efficiency, acceptance, and resolution effects cancel in the ratio.

It is of physical interest to evaluate the correlation function as a function of the relative momentum[2] $q \equiv p^a - p^b$ in intervals of average momentum $k \equiv \frac{1}{2}\left(p^a + p^b\right)$. The relative momentum distribution $A(q) \equiv \frac{dN}{dq}\Big|_{\text{same}}$ is formed by selecting pairs of particles from each event in an event class, which is defined by the collision centrality and z position of the primary vertex. The background $B(q) \equiv \frac{dN}{dq}\Big|_{\text{mix}}$ is constructed by event mixing, that is, by selecting one particle from each of two events in the same event class as $A(q)$. The ratio of the distributions defines the correlation function:

$$C_{\mathbf{k}}(q) \equiv \frac{A_{\mathbf{k}}(q)}{B_{\mathbf{k}}(q)}. \tag{2}$$

The relative momentum correlation functions are studied as a function of $q_{\text{inv}} \equiv \sqrt{-q_\mu q^\mu}$ and the three-vector $\mathbf{q}$. When working in all three dimensions, a longitudinally co-moving frame (LCMF) with the pair of particles is used such that $k_z = 0$. The coordinate axes are defined according to the "out-side-long" convention [39–41]:

$$q_{\text{out}} \equiv \frac{\mathbf{k}_T \cdot \mathbf{q}}{|\mathbf{k}_T|} = \frac{|\mathbf{p}_T^a|^2 - |\mathbf{p}_T^b|^2}{2k_{\text{T}}}, \tag{3}$$

$$q_{\text{side}} \equiv \frac{(\hat{\mathbf{z}} \times \mathbf{k}_T) \cdot \mathbf{q}}{|\mathbf{k}_T|} = -\frac{\hat{\mathbf{z}} \cdot \left(\mathbf{p}_T^a \times \mathbf{p}_T^b\right)}{k_{\text{T}}}, \tag{4}$$

$$q_{\text{long}} \equiv \hat{\mathbf{z}} \cdot \mathbf{q} = \frac{p_z^a E^b - p_z^b E^a}{\sqrt{k_0^2 - k_z^2}}. \tag{5}$$

[2] While q here refers to the relative four-momentum, it is also used generically to refer to either the Lorentz invariant q_{inv} or three-vector $\mathbf{q}$. The correlation function is studied in terms of both these variables but the description of the analysis is nearly identical for both cases.

3.5 Parameterization and fitting of the correlation function

In the approximation that all particles are identical pions created in a fully chaotic source and that they have no final-state interactions, the correlation function is enhanced by the Fourier transform of the source density. This description is useful for guiding intuition, but is not sufficient for a complete analysis. The Bowler-Sinyukov formalism [42, 43] is used to account for final-state corrections:

$$C_{\mathbf{k}}(q) = (1 - \lambda) + \lambda K(q) C_{\mathrm{BE}}(q)\,, \tag{6}$$

where K is a factor for final-state corrections, and $C_{\mathrm{BE}}(q) = 1 + \mathcal{F}\left[S_{\mathbf{k}}\right](q)$ with $\mathcal{F}\left[S_{\mathbf{k}}\right](q)$ denoting the Fourier transform of the two-particle source density function $S_{\mathbf{k}}(r)$. A number of factors influences the value of the experimental parameter λ, which is constrained between 0 and 1. Including non-identical particles decreases this parameter, as does coherent emission. Products of weak decays or long-lived resonances are emitted at a length scale greater than can be resolved by the momentum resolution of the detector, and also lead to a decrease in λ. These additional contributions to the source density are not Coulomb-corrected in the Bowler-Sinyukov form. When describing pion pairs of opposite charge, there is no Bose-Einstein enhancement and $C_{\mathrm{BE}} \to 1$.

The particular choice of the correction factor $K(q)$ is determined using the formalism in Ref. [44], under the approximation that the Coulomb correction is effectively applied over a Gaussian source density of radius R_{eff}:

$$K(q_{\mathrm{inv}}) = G(q_{\mathrm{inv}}) \left[1 + \frac{8R_{\mathrm{eff}}}{\sqrt{\pi}a} {}_2F_2\left(\frac{1}{2}, 1; \frac{3}{2}, \frac{3}{2}; -R_{\mathrm{eff}}^2 q_{\mathrm{inv}}^2\right)\right]\,, \tag{7}$$

where $G(q_{\mathrm{inv}})$ is the Gamow factor [45] $G(q_{\mathrm{inv}}) = \frac{4\pi}{a q_{\mathrm{inv}}} \left(e^{\frac{4\pi}{a q_{\mathrm{inv}}}} - 1\right)^{-1}$, $a = 388$ fm is the Bohr radius of two pions, and ${}_2F_2$ is a generalised hypergeometric function.

The Bose-Einstein enhancement in the correlation function is fit to an exponential form,

$$C_{\mathrm{BE}}(q) = 1 + e^{-||Rq||}\,, \tag{8}$$

where q refers to either q_{inv} or $\mathbf{q}$ depending on whether it is applied to the one- or three-dimensional correlation function, and R is a diagonal matrix in one or three dimensions whose components are the source radii. The double-bar expression $||Rq||$ indicates the vector magnitude of $R\mathbf{q}$ in three dimensions and the absolute value of $R_{\mathrm{inv}} q_{\mathrm{inv}}$ in one dimension. This function corresponds to an underlying Cauchy source density. A Gaussian enhancement is found to not describe the data as well as an exponential, which is also observed in the pp results in Ref. [26]. The choice of form for $\mathcal{F}[S_{\mathbf{k}}](\mathbf{q})$ must be taken into account when interpreting source radii, and there is no simple correspondence between results using one form and those using another.

A negative log-likelihood ratio $\mathcal{L}$ is minimised that assumes the bin contents of A and B are Poisson distributed and C is best fit to the ratio of their means:

$$-2\ln\mathcal{L} = 2\sum_i \left[A_i \ln\left(\frac{(1+C_i)A_i}{C_i(A_i+B_i+2)}\right) + (B_i+2)\ln\left(\frac{(1+C_i)(B_i+2)}{A_i+B_i+2}\right)\right]\,. \tag{9}$$

The factor -2 makes this statistic approach χ^2 in the high-statistics limit. Here A and B are the quantities in Eq. 2 when considered as histograms, such that A_i and B_i are the contents in bin i. C_i is shorthand for $C(q_i)$ where q_i is the bin centre and $C(q)$ is the fitting function describing the correlation. The statistical uncertainties in the fit parameters of $C(q)$ are selected from the points in the parameter space where $-2\ln\mathcal{L} = \min(-2\ln\mathcal{L}) + 1$.

4 Hard-process contribution

Additional non-femtoscopic enhancements to the correlation functions at $q_{\text{inv}} \lesssim 0.5-1$ GeV are observed in both $+-$ (opposite charge) and $\pm\pm$ (same charge) pairs. This section describes the Monte Carlo (MC) generators used to study these structures and presents the study performed to constrain their description.

4.1 Monte Carlo generators

Four Monte Carlo generator-level samples are used to study the background described in this section at the truth level. No subsequent simulation is performed, as the effects of the reconstruction were studied using full simulation and found to be negligible. In each of the following samples, 50 million minimum-bias events are generated at a centre-of-mass energy per nucleon-nucleon pair of $\sqrt{s_{\text{NN}}} = 5.02$ TeV.

1. Hijing p+Pb [37]
   The same settings as in the nominal ATLAS p+Pb reconstructed simulation (as described in Sect. 3.2) are used, except that the minimum hard-scattering p_{T} is adjusted as described in Sect. 4.2. A boost is applied along the collision axis in the proton-going direction to match the frame of the measured p+Pb system.
2. Hijing pp
   The generator is run with all of the same settings as the p+Pb sample, except that both incoming particles are protons and no boost is applied.
3. Pythia 8 pp [46]
   The default ATLAS tune "UE AU2-CTEQ6L1" is used with Pythia 8.209, which utilises the CTEQ 6L1 parton distribution function (PDF) from LHAPDF6 [47].
4. Herwig ++ pp [48]
   The NNLO MRST PDF [49] was used with Herwig ++ 2.7.1.

4.2 Data-driven estimate of hard process backgrounds

The non-femtoscopic enhancement is more prominent at higher k_{T} and lower multiplicities. This suggests that the correlation is primarily due to jet fragmentation. This attribution is verified by studying correlation functions in Hijing where the contribution from jets can be removed by increasing the minimum hard-scattering p_{T} from 2 to 20 GeV, as demonstrated in Fig. 2.

The amplitude of the hard-process contribution tends to be larger in Monte Carlo generators than it is in the data. Thus, attempting to account for it by studying the double-ratio $C^{\text{data}}(q)/C^{\text{MC}}(q)$ leads to a depletion that is apparent in the region where the Bose-Einstein enhancement disappears [26]. Another

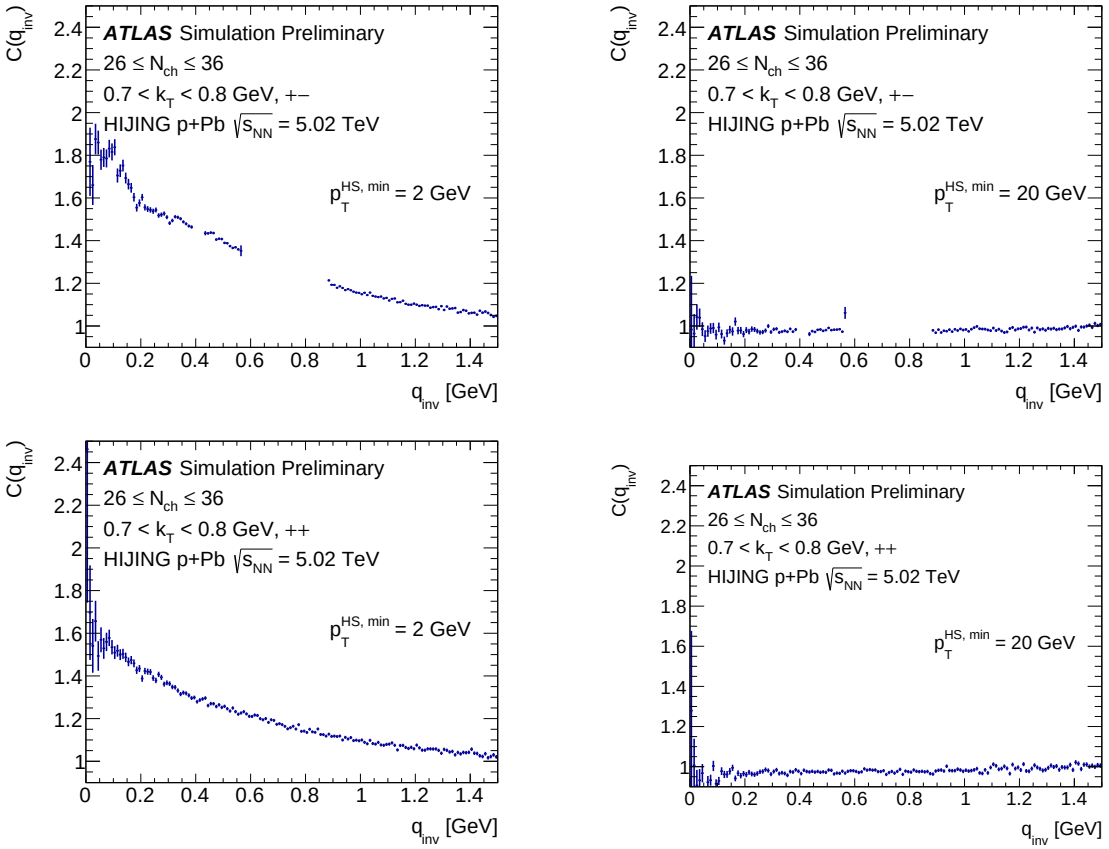

Figure 2: Correlation functions of truth-level charged particles from HIJING for +− pairs (top) and ++ pairs (bottom). The generator is run with the minimum hard-scattering $p_{\mathrm{T}}^{\mathrm{HS,\,min}}$ at the default setting of 2 GeV (left) and turned up to 20 GeV (right) to remove the contribution from hard processes. The gaps in the opposite-sign correlation functions are a result of the selections described in Sect. 3.3, which remove the largest resonance contributions.

commonly used method is to parameterize the mini-jet contribution using MC and allow one or more parameters of the description to be free in the fit [31, 32].

The analysis presented in this note avoids both of these strategies and instead develops a data-driven method to constrain the correlations from jet fragmentation. Opposite-sign correlation functions are used to predict the jet contribution in the same-sign correlation function. This has two clear difficulties. Firstly, resonance decays appear prominently in the opposite-sign correlations. The most prominent of these are removed by selections on the invariant mass of the opposite-sign pairs (as described in Sect. 3.3), and the fits ignore opposite-sign structure below $q_{\mathrm{inv}} = 0.2$ GeV. Secondly, jet fragmentation affects the opposite-sign correlations at a different level than it does for same-sign pairs. This is in part because opposite-sign pairs are more likely to have a closer common ancestor in a jet's fragmentation into hadrons.

To account for the remaining differences between +− and ±± pairs, a study of the correlation function comparison is performed in PYTHIA 8. HIJING, which uses PYTHIA 6, was found to describe the charge comparison inadequately. Fits are performed to a stretched exponential function of the form

$$C(q_{\mathrm{inv}}) = \mathcal{N}\left(1 + \lambda_{\mathrm{bkgd}} e^{-|R_{\mathrm{bkgd}} q_{\mathrm{inv}}|^{\alpha_{\mathrm{bkgd}}}}\right), \tag{10}$$

where $\mathcal{N}$ is a normalization factor and the other parameters depend on the charge combination and on k_{T}. First, α_{bkgd} is determined with fits to same-sign correlation functions. The fits are well described by a Gaussian form ($\alpha_{\mathrm{bkgd}} = 2$) at $k_{\mathrm{T}} \lesssim 0.4$ GeV. The shape parameter α_{bkgd} is only very weakly dependent on multiplicity, so a function is fit to parameterize α_{bkgd} as a function of k_{T}. The fits to correlation functions are performed again with α_{bkgd} fixed to the same value in same- and opposite-charged pairs, and a comparison is made between the width parameters R^{+-}_{bkgd} and $R^{\pm\pm}_{\mathrm{bkgd}}$. The width of the jet fragmentation correlation for same-sign pairs is found to be roughly proportional to that for opposite-sign pairs:

$$R^{\pm\pm}_{\mathrm{bkgd}} = \rho R^{+-}_{\mathrm{bkgd}} \,. \tag{11}$$

This proportionality begins to break down at low k_{T}, but in this kinematic region hard processes contribute little to the correlation function (i.e. λ_{bkgd} is small). The multiplicity of charged particles, N_{ch}, is the number of truth-level charged particles for $p_{\mathrm{T}} > 0.1$ GeV and $|\eta| < 2.5$. The ρ parameter is extracted as a k_{T}- and multiplicity-independent factor. Finally, $R^{\pm\pm}_{\mathrm{bkgd}}$ is also fixed from R^{+-}_{bkgd} using the value of ρ, and the fits are performed again to parameterize the relationship between the amplitudes:

$$\lambda^{\pm\pm}_{\mathrm{bkgd}} = \mu(k_{\mathrm{T}}) \left(\lambda^{+-}_{\mathrm{bkgd}}\right)^{\nu(k_{\mathrm{T}})} \,. \tag{12}$$

At each k_{T}, μ and ν are fit to describe four multiplicity intervals ($26 \leq N_{\mathrm{ch}} \leq 36$, $37 \leq N_{\mathrm{ch}} \leq 48$, $49 \leq N_{\mathrm{ch}} \leq 64$, and $65 \leq N_{\mathrm{ch}}$). The power-law scaling of Eq. 12 is found to provide a good description of the relation between the same- and opposite-sign amplitudes across all four multiplicity intervals studied. The multiplicity-independence of μ and ν is important to justify the use of these parameters in p+Pb.

Since this study is done with Pythia 8 in a pp system, Hijing is also used to compare the correspondence between opposite- and same-sign pairs in both pp and p+Pb. While the mapping is mostly consistent between the two systems, it is found that μ is larger in p+Pb than in pp by 8.5% on average. When the mapping is applied to the data, this factor is also taken into account, and the standard deviation of this factor is incorporated into a systematic uncertainty.

With $\alpha_{\mathrm{bkgd}}(k_{\mathrm{T}})$, $\mu(k_{\mathrm{T}})$, $\nu(k_{\mathrm{T}})$, and ρ determined from generator-level samples, the mapping can be applied to the p+Pb data. As illustrated in Fig. 3, the $+-$ correlation function is fit to Eq. 10 for $q_{\mathrm{inv}} > 0.2$ GeV, with α_{bkgd} fixed from Pythia 8 and $\lambda^{+-}_{\mathrm{bkgd}}$ and R^{+-}_{bkgd} as free parameters. The μ, ν, and ρ are used to infer $\lambda^{\pm\pm}_{\mathrm{bkgd}}$ and $R^{\pm\pm}_{\mathrm{bkgd}}$, which are fixed before the femtoscopic part of the correlation function is fit to $\pm\pm$ data.

In three dimensions, q_{inv} is calculated from $\mathbf{q}$ and the average k_{T} in each bin. The same parameters used to describe the hard-process contribution in the invariant correlation function are also used in the 3D fit.

The full form of the correlation function fit to $\pm\pm$ data including the hard-process background description is

$$C(q) = \mathcal{N}\left[1 - \lambda + \lambda K(q_{\mathrm{inv}}) C_{\mathrm{BE}}(q)\right] \left(1 + \lambda^{\pm\pm}_{\mathrm{bkgd}} e^{-|R^{\pm\pm}_{\mathrm{bkgd}} q_{\mathrm{inv}}|^{\alpha_{\mathrm{bkgd}}}}\right) , \tag{13}$$

where q refers generically to either q_{inv} or $\mathbf{q}$.

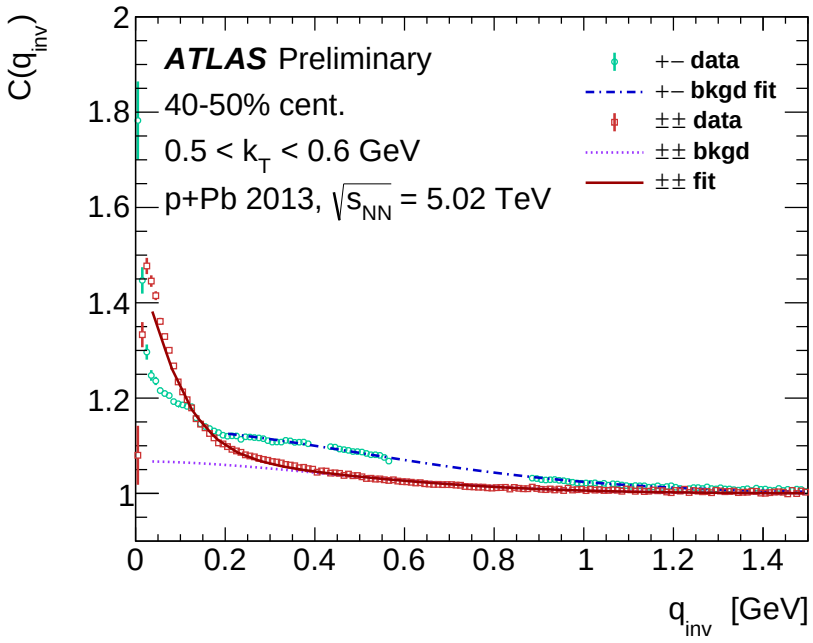

Figure 3: Correlation functions in p+Pb data for opposite-sign (teal circles) and same-sign (red squares) pairs. The opposite-sign correlation function, with the most prominent resonances removed, is fit to a function of the form in Eq. 10 (blue dashed line). The violet dotted line is the estimation of the jet contribution in the same-sign correlation function, also of the form of Eq. 10, and the dark red line is the full fit of Eq. 13 to the same-sign data.

5 Systematic uncertainties

Systematic uncertainties are determined to account for the hard-process background description, PID, the effective Coulomb correction size R_{eff}, charge asymmetry, and two-particle effects.

One of the largest sources of uncertainty in femtoscopy in small systems in high-energy collisions comes from forming an accurate description of the background contribution from hard processes. For the uncertainty in the hard-process contribution three effects are considered. The variation in the translation from pp to p+Pb is taken as an uncertainty in the amplitude, as mentioned in Sect. 4. Additionally, the amplitude of $C^{+-}(q_{\text{inv}})/C^{\pm\pm}(q_{\text{inv}})$ is studied in both Pythia and Herwig. Herwig predicts not nearly enough difference between $+-$ and $\pm\pm$ to describe the data. Thus, instead of using the ratio between the two generators' predicted scalings, the standard deviation of the ratio amplitude (across a selection of k_{T} and multiplicity intervals) is used as a systematic variation. The hard-process amplitude λ_{bkgd} is scaled up and down by 12.3%, the quadrature sum of the relative variation from the pp to p+Pb distinction (4.1%) and from the generator difference (11.6%). Additionally, in three-dimensional fits the mini-jet contribution is described by mapping $\mathbf{q}$ onto q_{inv}, which uses the average k_{T} in the interval. The choice of k_{T} is varied up and down by one standard deviation of the values in that k_{T} interval (typically about 30 MeV).

The analysis is repeated at both a looser and a tighter PID selection definition, and the variation is included as a systematic uncertainty. The effect on the radii is at the 1-2% level for the lower k_{T} intervals, but becomes more significant at higher momentum intervals, where there are relatively more kaons and protons and the dE/dx separation is not as good.

k_T [GeV]	0.1–0.2	0.2–0.3	0.3–0.4	0.4–0.5	0.5–0.6	0.6–0.7	0.7–0.8
λ_{bkgd}	3.1%	2.8%	4.4%	5.4%	7.8%	11%	16%
Effective Coulomb size R_{eff}	4.6%	5.2%	5.4%	4.3%	3.9%	3.7%	3.6%
Pion identification	0.1%	0.21%	0.43%	1.3%	1%	3.2%	2.1%
Charge asymmetry	1%	0.37%	0.29%	0.13%	1.3%	2.6%	1.6%
Minimum q in fit	0.45%	0.44%	0.98%	0.68%	1.3%	1.5%	0.54%
All	5.6%	5.9%	7.1%	7.1%	9%	12%	16%

Table 1: The relative systematic uncertainties in R_{inv} in the 1-5% centrality interval. The quadrature average of the upper and lower systematic errors is divided by the nominal value to compute the relative uncertainty. The uncertainty is dominated by the hard-process background description and the contribution from the effective Coulomb size R_{eff} is also significant at low k_T.

k_T [GeV]	0.1–0.2	0.2–0.3	0.3–0.4	0.4–0.5	0.5–0.6	0.6–0.7	0.7–0.8
λ_{bkgd}	2%	3.7%	6.6%	9.4%	12%	16%	20%
Effective Coulomb size R_{eff}	1.4%	1.2%	0.98%	0.86%	0.87%	0.83%	0.74%
Pion identification	1.1%	2.7%	4.7%	4.2%	3.8%	4.1%	3.4%
Charge asymmetry	0.66%	0.73%	0.069%	0.83%	0.087%	2.2%	1.8%
Minimum q in fit	0.82%	1.2%	1.5%	1.7%	0.71%	0.68%	0.42%
All	2.9%	4.9%	8.3%	11%	13%	16%	20%

Table 2: The relative systematic uncertainties in R_{inv} for the 60-70% centrality interval, as in Table 1. The uncertainty is dominated by the hard-process background description.

The non-zero effective size of the Coulomb correction R_{eff} should only provide a bin-by-bin difference of a few percent, even with a value up to several fm, since the Bohr radius of pions is nearly 400 fm. However, since the parameter changes the q_{inv} width over which the Coulomb correction is applied, varying this parameter can affect the source radii from around 1% (peripheral) to 6% (central). The nominal value of 3 fm lies in the middle of the measured radii. The R_{eff} is varied down to 1 fm and up to 6 fm, and the change in the radii is included in the systematic uncertainties. This range is chosen as a conservative estimate, as it encompasses the majority of the results.

A small difference between positive and negative charge pairs is observed, attributable to detector effects such as the orientation of the overlap of the inner detector component staves. The nominal results use all of the same-sign pairs, and a systematic variation accounting for this charge asymmetry is chosen to overlap the results for both of the separate charge states.

Single-particle correction factors cancel out in the ratio $A(q)/B(q)$. However, two-particle effects on the track reconstruction can affect the correlation function. In the reconstructed HIJING sample, the truth-level and reconstructed correlation functions are compared, and a depletion in the first few q_{inv} bins is observed. A minimum q cutoff is applied in the fits to avoid being affected by these detector effects. The sensitivity of the results to this limit is checked by taking $q_{inv}^{min} = 30 \pm 10$ MeV in the 1D fits, and symmetrising the effect of the variation from $|\mathbf{q}|^{min} = 25$ to 50 MeV in the 3D fits.

The relative systematic uncertainties in R_{inv} are shown for a central interval (1-5%) in Table 1 and a peripheral interval (60-70%) in Table 2. The relative systematic uncertainties are also tabulated for the 3D radii R_{out} (Table 3), R_{side} (Table 4), and R_{long} (Table 5) averaged over centrality.

k_T [GeV]	0.1–0.2	0.2–0.3	0.3–0.4	0.4–0.5	0.5–0.6	0.6–0.7	0.7–0.8
λ_{bkgd}	2%	3%	4.4%	6.9%	8.2%	9.8%	13%
Effective Coulomb size R_{eff}	3.5%	4.2%	4.7%	5.1%	4.5%	3.6%	2.2%
Pion identification	0.51%	1.2%	1.6%	1.5%	1.5%	4.5%	17%
Charge asymmetry	1.4%	1.4%	0.93%	0.87%	1.2%	1.3%	1.1%
Minimum q in fit	1.3%	1.4%	0.75%	0.37%	0.17%	0.24%	0.67%
k_T in background	0.18%	0.89%	0.31%	0.28%	0.17%	0.11%	0.16%
All	5%	6.4%	7.4%	9.2%	9.9%	12%	22%

Table 3: The relative systematic uncertainties in R_{out}, averaged over centrality. The quadrature average of the upper and lower systematic errors is divided by the central value, which is averaged equally over centrality intervals from 0% to 80%. The values in the "All" row are averaged over centrality in the same way but include all systematic variations added in quadrature.

k_T [GeV]	0.1–0.2	0.2–0.3	0.3–0.4	0.4–0.5	0.5–0.6	0.6–0.7	0.7–0.8
λ_{bkgd}	1.6%	2.5%	3.5%	5.3%	6.6%	8.4%	11%
Effective Coulomb size R_{eff}	2.5%	2.4%	2.4%	2.3%	2%	2.2%	3.1%
Pion identification	0.25%	0.84%	1.2%	1.4%	1.9%	7.2%	34%
Charge asymmetry	0.97%	0.85%	0.47%	1%	1.4%	1.6%	3%
Minimum q in fit	0.47%	0.85%	0.49%	0.33%	0.22%	0.27%	0.93%
k_T in background	0.045%	0.44%	0.097%	0.11%	0.27%	0.55%	1.2%
All	3.3%	4.1%	4.8%	6.2%	7.4%	12%	36%

Table 4: The relative systematic uncertainties in R_{side}, averaged over centrality in the same manner as in Table 3.

k_T [GeV]	0.1–0.2	0.2–0.3	0.3–0.4	0.4–0.5	0.5–0.6	0.6–0.7	0.7–0.8
λ_{bkgd}	1.8%	2.8%	3.5%	5%	6.1%	7.9%	11%
Effective Coulomb size R_{eff}	3.2%	3%	2.6%	2.2%	1.8%	1.6%	2.3%
Pion identification	0.5%	0.95%	0.93%	0.78%	1.4%	5.2%	24%
Charge asymmetry	0.77%	0.81%	0.46%	0.75%	1.2%	1.1%	2%
Minimum q in fit	0.38%	0.8%	0.42%	0.27%	0.21%	0.24%	0.63%
k_T in background	0.043%	0.52%	0.076%	0.11%	0.26%	0.52%	1.1%
All	4.1%	4.8%	4.9%	5.8%	6.8%	9.9%	27%

Table 5: The relative systematic uncertainties in R_{long}, averaged over centrality in the same manner as in Table 3.

6 Results

This section first shows examples of fits to correlation functions and discusses the evaluation of two quantities, $\langle dN_{\rm ch}/d\eta \rangle$ and $\langle N_{\rm part} \rangle$, for each centrality interval. The remainder of the section presents results for extracted invariant and 3D source radii as a function of $k_{\rm T}$, $\langle dN_{\rm ch}/d\eta \rangle$, and $\langle N_{\rm part} \rangle$.

6.1 Fit examples

An example of a fit to $C(q_{\rm inv})$ was included in Fig. 3, using the functional form of Eq. 13. The fit in the same-sign correlation function reasonably describes the data, although the statistical uncertainties are so small that a small departure of the correlation function from the exponential description can be detected. Slices of a three-dimensional (3D) fit of $C(\mathbf{q})$ to the three-dimensional variant of Eq. 13 are shown in Fig. 4. The apparently imperfect fit along the $q_{\rm out}$ axis is characteristic of $q_{\rm side} \approx q_{\rm long} \approx 0$, and away from this slice the agreement of the fit with the data improves.

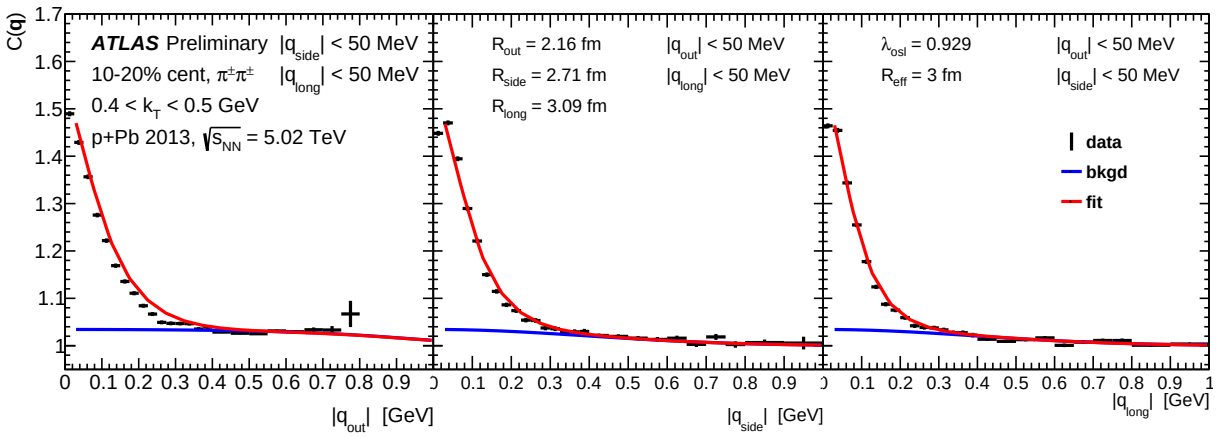

Figure 4: Example of the 3D fit showing slices along each axis in $\mathbf{q}$-space. The blue line indicates the description of the contribution from hard processes and the red line shows the full correlation function fit. The test statistic $-2\ln\mathcal{L} = 22369$ and there are 19805 degrees of freedom in the fit.

6.2 Centrality: $N_{\rm part}$ and average multiplicity

The mean $N_{\rm part}$ ($\langle N_{\rm part} \rangle$) in each centrality interval is extracted using the procedure in Ref. [35]. The values used for $\langle N_{\rm part} \rangle$ are shown in Table 6 for each of the three models evaluated. The Glauber $\langle N_{\rm part} \rangle$ are also used to perform a linear interpolation for $\langle dN_{\rm ch}/d\eta \rangle$ in finer centrality intervals than those available in Ref. [35]. The interpolation is justified with the result in Ref. [35] that charged particle multiplicity is proportional to $\langle N_{\rm part} \rangle$ in the peripheral region. The average charged particle multiplicities within $|\eta| < 1.5$ that are extracted using this interpolation are also shown in Table 6.

Centrality	$\langle N_{\rm part}\rangle^{\rm Glauber}$	$\langle N_{\rm part}\rangle^{\rm GGCF}$ $\omega_\sigma = 0.11$	$\langle N_{\rm part}\rangle^{\rm GGCF}$ $\omega_\sigma = 0.2$	$\langle dN_{\rm ch}/d\eta\rangle$
0–1%	$18.22^{+2.62}_{-1.01}$	$24.18^{+1.52}_{-2.07}$	$27.42^{+1.58}_{-4.48}$	$58.07 \pm 0.09 \pm 1.86$
1–5%	$16.10^{+1.66}_{-0.90}$	$19.52^{+1.24}_{-1.32}$	$21.41^{+1.46}_{-1.98}$	$45.78 \pm 0.09 \pm 1.33$
5–10%	$14.61^{+1.21}_{-0.82}$	$16.49^{+1.00}_{-1.00}$	$17.46^{+1.13}_{-1.08}$	$38.53 \pm 0.06 \pm 1.12$
10–20%	$13.05^{+0.82}_{-0.73}$	$13.77^{+0.79}_{-0.81}$	$14.11^{+0.86}_{-0.79}$	$32.34 \pm 0.05 \pm 0.97$
20–30%	$11.37^{+0.65}_{-0.63}$	$11.23^{+0.62}_{-0.67}$	$11.17^{+0.68}_{-0.62}$	$26.74 \pm 0.04 \pm 0.80$
30–40%	$9.81^{+0.56}_{-0.57}$	$9.22^{+0.50}_{-0.54}$	$8.97^{+0.60}_{-0.49}$	$22.48 \pm 0.03 \pm 0.75$
40–50%	$8.23^{+0.48}_{-0.55}$	$7.46^{+0.41}_{-0.43}$	$7.15^{+0.54}_{-0.39}$	$18.79 \pm 0.02 \pm 0.69$
50–60%	$6.64^{+0.41}_{-0.52}$	$5.90^{+0.36}_{-0.34}$	$5.60^{+0.47}_{-0.30}$	$15.02 \pm 0.02 \pm 0.62$
60–70%	$5.14^{+0.35}_{-0.43}$	$4.56^{+0.32}_{-0.26}$	$4.32^{+0.41}_{-0.23}$	$11.45 \pm 0.01 \pm 0.56$
70–80%	$3.90^{+0.24}_{-0.30}$	$3.5^{+0.22}_{-0.18}$	$3.34^{+0.29}_{-0.16}$	$8.49 \pm 0.02 \pm 0.51$

Table 6: $\langle N_{\rm part}\rangle$ for each centrality interval in the Glauber model as well as the two choices for the Glauber-Gribov model with colour fluctuations (GGCF), along with the average multiplicity within $|\eta| < 1.5$. Asymmetric systematic uncertainties are shown for $\langle N_{\rm part}\rangle$. The uncertainties in $\langle dN_{\rm ch}/d\eta\rangle$ are given in the order of statistical followed by systematic.

6.3 One-dimensional results

The results from fits of $C(q_{\rm inv})$ to Eq. 13 for the invariant radius $R_{\rm inv}$ are shown in Fig. 5 in four selected centrality intervals. The clear decrease in size with increasing $k_{\rm T}$ that is observed in central events is not significant in peripheral events. Taken at face value, this suggests that central events undergo transverse expansion, since in hydrodynamic models higher-$p_{\rm T}$ particles are more likely to freeze out earlier in the event. Another way of understanding this trend as evidence for transverse expansion is that there is a smaller homogeneity region for particles with higher $p_{\rm T}$ [30]. At low $k_{\rm T}$, ultra-central (0-1%) events have an invariant radius significantly greater than peripheral (70-80%) events by a factor of about 2.6. This difference becomes less prominent at high $k_{\rm T}$.

Invariant radii are also shown for all centralities in Fig. 6, as a function of the cube root of average $dN_{\rm ch}/d\eta$. For both $k_{\rm T}$ intervals shown, the scaling of $R_{\rm inv}$ with $\langle dN_{\rm ch}/d\eta\rangle^{1/3}$ is close to linear but with a slightly increasing slope at higher multiplicities. $R_{\rm inv}$ has a steeper trend versus multiplicity at lower $k_{\rm T}$.

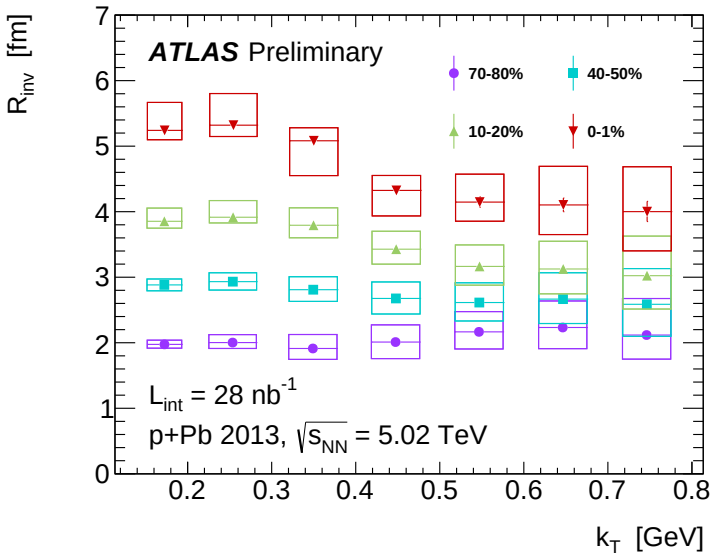

Figure 5: The exponential invariant radii $R_{\rm inv}$ as a function of $k_{\rm T}$. The vertical sizes of the boxes are the quadrature sum of the systematic uncertainties described in Sect. 5, and statistical uncertainties are shown with vertical lines. The horizontal positions of the boxes are the average $k_{\rm T}$ in each interval, and the widths of the boxes indicate the standard deviation of $k_{\rm T}$.

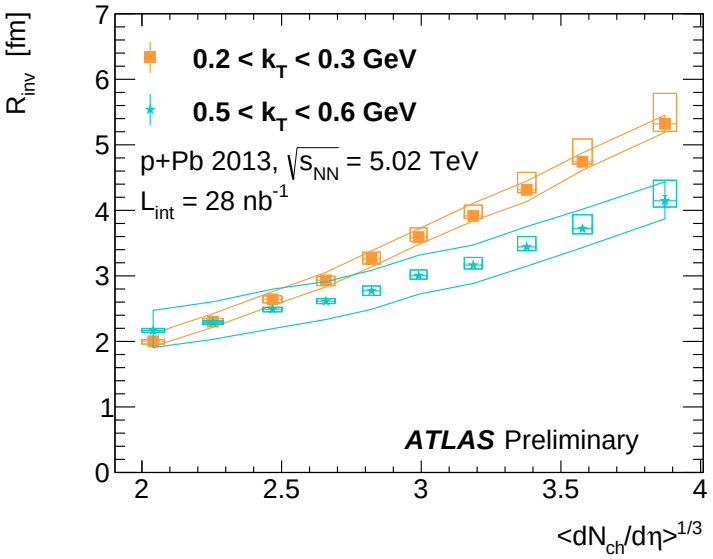

Figure 6: Exponential fit results for $R_{\rm inv}$ as a function of the cube root of average charged particle multiplicity, $\langle dN_{\rm ch}/d\eta\rangle^{1/3}$, where the average is taken over $|\eta| < 1.5$. The systematic uncertainties from the background amplitude and pion identification are shown as error bands while the systematics from charge asymmetry, $R_{\rm eff}$, and q-cutoff are indicated by the height of the boxes. The horizontal error bars indicate the systematic uncertainty from $\langle dN_{\rm ch}/d\eta\rangle$ as tabulated in Sect. 6.2.

6.4 Three-dimensional results

The three-dimensional radii $R_{\rm out}$, $R_{\rm side}$, and $R_{\rm long}$ are shown as a function of $k_{\rm T}$ in a selection of four centrality intervals in Fig. 7. The 3D radii exhibit an even steeper drop-off from low to high $k_{\rm T}$ in central events relative to what is observed for the invariant radii in Fig. 5. This trend is present, but not as strong, in peripheral events.

The radii are also shown as a function of the cube root of average multiplicity in Fig. 8, which probes the relationship between the size and the source density at freeze-out. Linear scaling is observed with different intercepts at different values of $k_{\rm T}$, in a qualitatively similar way to the scaling of $R_{\rm inv}$ with $\langle dN_{\rm ch}/d\eta \rangle$ in Fig. 6.

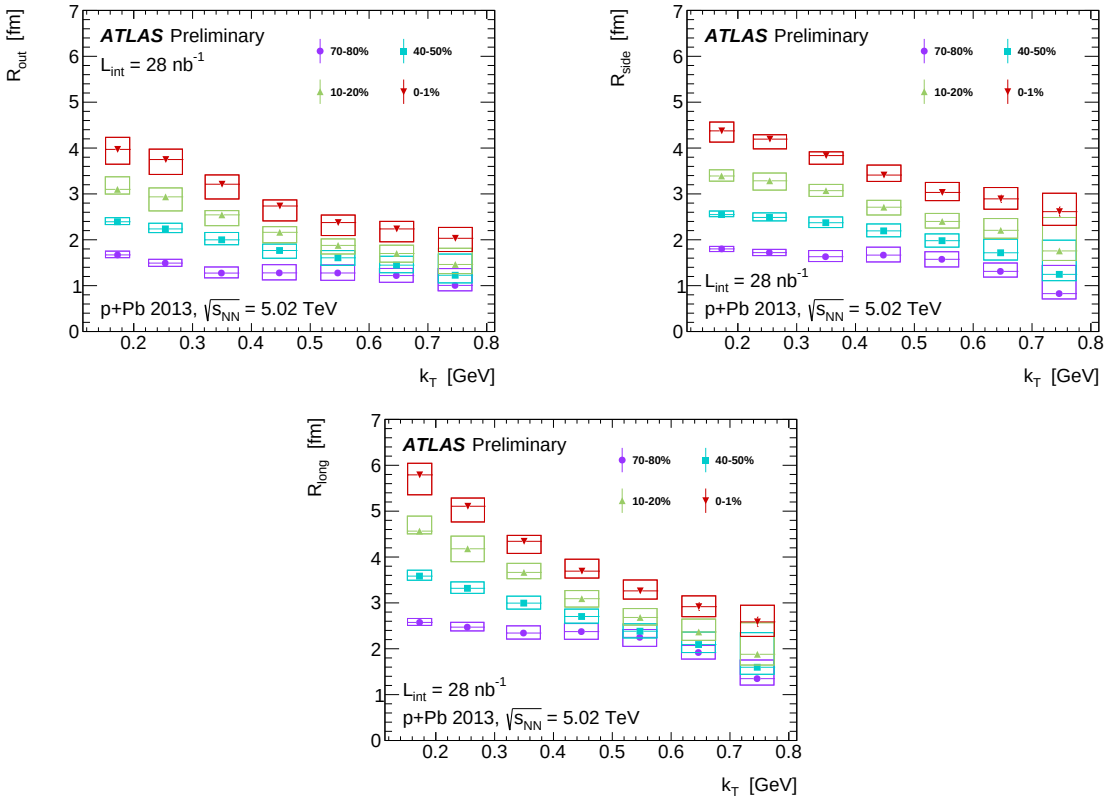

Figure 7: Exponential fit results for 3D source radii as a function of $k_{\rm T}$. A selection of four non-adjacent centrality intervals are shown. The vertical size of the boxes are the quadrature sum of the systematic uncertainties described in Sect. 5, and statistical uncertainties are shown with vertical lines. The horizontal positions of the boxes are the average $k_{\rm T}$ in each interval, and the widths of the boxes indicate the standard deviation of $k_{\rm T}$.

The ratio $R_{\rm out}/R_{\rm side}$ (Fig. 9) is often of interest since, in models with radial flow, $R_{\rm out}$ includes components of the source's lifetime but $R_{\rm side}$ does not (see, for instance, the discussion in [1]). A value of $R_{\rm out}/R_{\rm side}$ less than 1 is observed with a decrease at increasing $k_{\rm T}$. In the region where the systematic uncertainties are small, the ratio is observed to remain constant over centrality. As explained in [50], several improvements to naive hydrodynamic models—primarily pre-thermal acceleration, a stiffer equation of state, and shear viscosity—all result in more sudden emission. Thus, a value of $R_{\rm out}/R_{\rm side} \lesssim 1$ does not necessarily rule out collective behaviour.

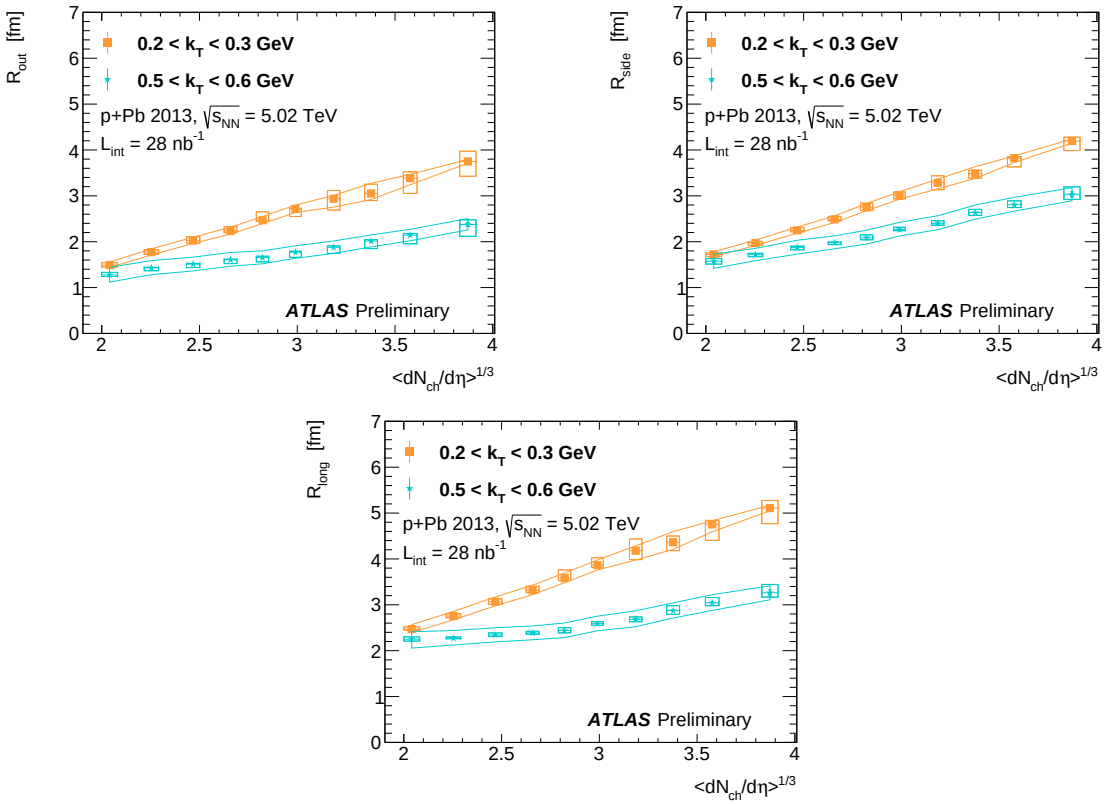

Figure 8: The scaling of the 3D exponential radii with the cube root of charged-particle multiplicity. Systematic uncertainties from the hard-process description and pion identification are shown in bands while those from charge asymmetry, R_{eff}, and the minimum cutoff in the fits are represented by the height of the boxes. Statistical uncertainties are included but are smaller than the markers. The horizontal error bars indicate the systematic uncertainty from $\langle dN_{\mathrm{ch}}/d\eta \rangle$ as tabulated in Sect. 6.2.

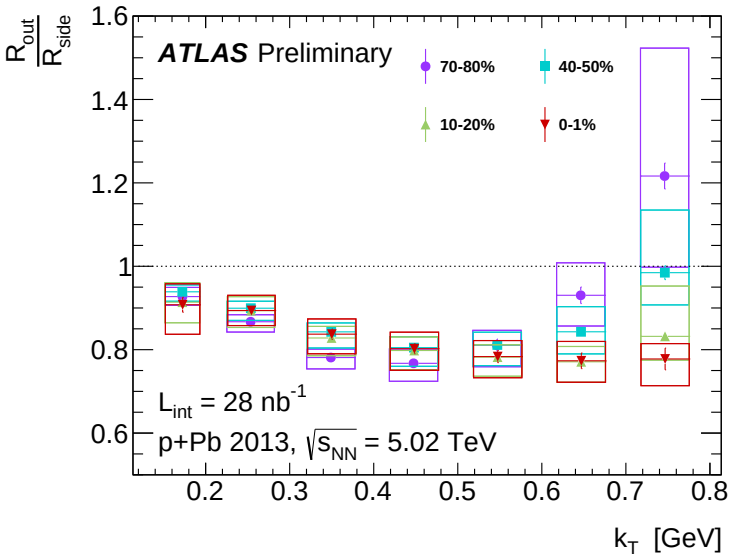

Figure 9: The ratio of exponential radii $R_{\rm out}/R_{\rm side}$ as a function of $k_{\rm T}$. The vertical size of the boxes are the quadrature sum of the systematic uncertainties described in Sect. 5, and statistical uncertainties are shown with vertical lines. The horizontal positions of the boxes are the average $k_{\rm T}$ in each interval, and the widths of the boxes indicate the standard deviation of $k_{\rm T}$.

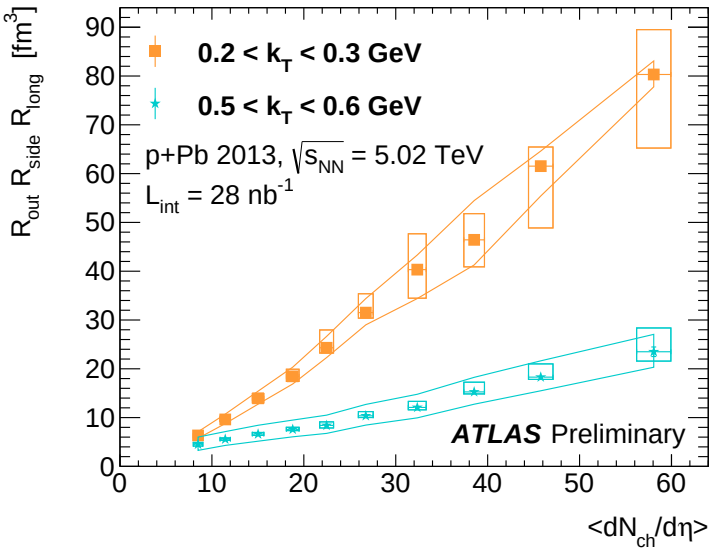

Figure 10: The product $R_{\rm out}R_{\rm side}R_{\rm long}$ for two $k_{\rm T}$ intervals plotted against the average multiplicity. The systematic uncertainties from the background description and pion identification are shown as error bands while the systematic uncertainties from charge asymmetry, $R_{\rm eff}$, and q-cutoff are indicated by the height of the boxes. The horizontal error bars indicate the systematic uncertainty from $\langle dN_{\rm ch}/d\eta\rangle$ as tabulated in Sect. 6.2.

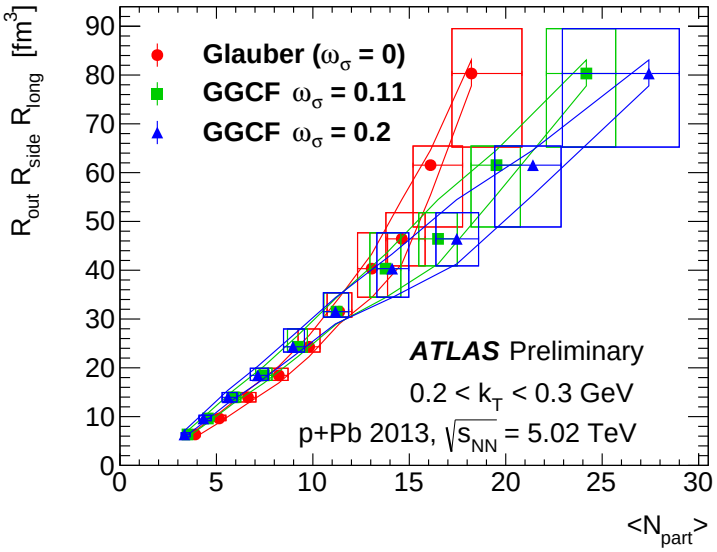

Figure 11: The scaling of the product $R_{\rm out}R_{\rm side}R_{\rm long}$ with $\langle N_{\rm part}\rangle$ calculated with three initial geometry models: standard Glauber as well as Glauber-Gribov (GGCF) for two choices of the colour fluctuation parameter ω_σ. The systematic uncertainties from the background description and pion identification are shown as error bands while the systematics from charge asymmetry, $R_{\rm eff}$, and q-cutoff are indicated by the height of the boxes. The horizontal error bars indicate the systematic uncertainties in $\langle N_{\rm part}\rangle$ as tabulated in Sect. 6.2.

The product of 3D radius parameters, $R_{\rm out}R_{\rm side}R_{\rm long}$, is shown in Fig. 10 as a function of the average multiplicity. The scaling of the volume with the multiplicity is nearly linear, which implies a constant freeze-out density. Fig. 11 compares the volume scaling with $\langle N_{\rm part}\rangle$ for the standard Glauber model as well as for two choices of the Glauber-Gribov colour fluctuation (GGCF) model [51]. The parameter ω_σ controls fluctuations in the nucleon-nucleon cross section within the Glauber-Gribov model. It is observed that a model that includes non-zero fluctuations in the proton size must be used in order to maintain a linear scaling of the volume with $\langle N_{\rm part}\rangle$. At $k_{\rm T} > 0.6$ GeV, this linear scaling no longer holds even for the $\omega_\sigma = 0.2$ model. The values and systematic uncertainties for $\langle N_{\rm part}\rangle$ in each model are listed in Sect. 6.2.

7 Summary and conclusions

Bose-Einstein correlations of identified pions are used to image the freeze-out source density of p+Pb collisions at $\sqrt{s_{\rm NN}} = 5.02$ TeV with ATLAS. Correlation functions in relative momentum space are fit to extract source radii as a function of collision centrality and pair $k_{\rm T}$. A data-driven technique is developed for constraining the contribution of jet fragmentation in the correlation function. The measured radii are observed to decrease with increasing $k_{\rm T}$ in central events, a pattern consistent with collective expansion. This decrease is found to be weaker in peripheral events. The ratio $R_{\rm out}/R_{\rm side}$ is observed to be less than one, suggestive of an explosive evolution of the source. Linear scaling of $R_{\rm out}R_{\rm side}R_{\rm long}$ with average charged particle multiplicity is observed, which implies a constant freeze-out density. With a model of the initial collision geometry that incorporates fluctuations in the size of the proton, a linear scaling of the source volume with $\langle N_{\rm part}\rangle$ is observed.

References

[1] M. A. Lisa et al., Ann. Rev. Nucl. Part. Sci. **55** (2005) 357–402.

[2] STAR Collaboration, Phys. Rev. Lett. **86** (3 2001) 402–407.

[3] PHENIX Collaboration, Phys. Rev. **C78** (2008) 014901.

[4] PHOBOS Collaboration, Phys. Rev. Lett. **104** (2010) 062301.

[5] ALICE Collaboration, Phys. Rev. Lett. **107** (3 2011) 032301.

[6] CMS Collaboration, JHEP **07** (2011) 076.

[7] ATLAS Collaboration, Phys. Rev. **C86** (2012) 014907.

[8] ATLAS Collaboration, Phys. Rev. **C90**.4 (2014) 044906.

[9] CMS Collaboration, Phys. Lett. **B718** (2013) 795–814.

[10] ALICE Collaboration, Phys. Lett. **B719** (2013) 29–41.

[11] ATLAS Collaboration, ATLAS-CONF-2015-027 (2015), URL: https://cds.cern.ch/record/2037663.

[12] CMS Collaboration, JHEP **09** (2010) 091.

[13] P. Bożek, Phys. Rev. C **85** (1 2012) 014911.

[14] E. Shuryak and I. Zahed, Phys. Rev. C **88** (4 2013) 044915.

[15] P. Bożek and W. Broniowski, Phys. Rev. C **88** (1 2013) 014903.

[16] G.-Y. Qin and B. Müller, Phys. Rev. C **89** (4 2014) 044902.

[17] K. Dusling and R. Venugopalan, Phys. Rev. D **87** (5 2013) 051502.

[18] K. Dusling and R. Venugopalan, Phys. Rev. D **87** (5 2013) 054014.

[19] Y. V. Kovchegov and D. E. Wertepny, Nucl. Phys. **A906** (2013) 50 –83.

[20] L. McLerran, M. Praszalowicz and B. Schenke, Nucl. Phys. **A916** (2013) 210 –218.

[21] K. Dusling and R. Venugopalan, Phys. Rev. D **87** (9 2013) 094034.

[22] A. Bzdak et al., Phys. Rev. C **87** (6 2013) 064906.

[23] R Hanbury Brown and R. Twiss, Nature **178** (1956) 1046–1048.

[24] R. Hanbury Brown and R. Twiss, Phil. Mag. **45** (1954) 663.

[25] G. Goldhaber et al., Phys. Rev. **120** (1 1960) 300–312.

[26] ATLAS Collaboration (2015), arXiv: 1502.07947 [hep-ex].

[27] CMS Collaboration, JHEP **05** (2011) 029.

[28] ALICE Collaboration, Phys. Rev. **D84** (2011) 112004.

[29] R. Lednicky, River Edge, USA: World Scientific (2003) 433 p (2003), arXiv: nucl-th/0212089.

[30] P. F. Kolb and U. W. Heinz (2003), arXiv: nucl-th/0305084 [nucl-th].

[31] ALICE Collaboration, Phys. Rev. C **91** (3 2015) 034906.

[32] ALICE Collaboration, Phys. Lett. **B739** (2014) 139–151.

[33] ATLAS Collaboration, JINST **3** (2008) S08003.

[34] ATLAS Collaboration, Eur. Phys. J. **C72** (2012) 1849.

[35] ATLAS Collaboration (2015), arXiv: 1508.00848 [hep-ex].

[36] ATLAS Collaboration, ATLAS-CONF-2011-016, 2011,
URL: https://cds.cern.ch/record/1336519.

[37] M. Gyulassy and X.-N. Wang, Comput. Phys. Commun. **83** (1994) 307.

[38] S. Agostinelli et al., Nucl. Instrum. Meth. **A506**.3 (2003) 250 –303.

[39] S. Pratt, Phys. Rev. D **33** (5 1986) 1314–1327.

[40] G. F. Bertsch, Nucl. Phys. **A498** (1989) 173 –179.

[41] T. Csorgo et al., Phys. Lett. **B241** (1990) 301–307.

[42] M. Bowler, Phys. Lett. **B270** (1991) 69–74.

[43] Y. Sinyukov et al., Phys. Lett. **B432** (1998) 248–257.

[44] R. Maj and S. Mrowczynski, Phys. Rev. **C80** (2009) 034907.

[45] L. Schiff, *Quantum Mechanics*, New York: McGraw-Hill, 1968.

[46] T. Sjostrand, S. Mrenna and P. Z. Skands, Comput. Phys. Commun. **178** (2008) 852–867.

[47] A. Buckley et al., Eur. Phys. J. **C75**.3 (2015) 132.

[48] M. Bahr et al., Eur. Phys. J. **C58** (2008) 639–707.

[49] A. D. Martin et al., Phys. Lett. **B531** (2002) 216–224.

[50] S. Pratt, Phys. Rev. Lett. **102** (2009) 232301.

[51] M. Alvioli and M. Strikman, Phys. Lett. **B722** (2013) 347–354.